Cite this: *J. Mater. Chem. A*, 2020, **8**, 8421

Testing the predictive power of theory for Pd_xIr_(100-x) alloy nanoparticles for the oxygen reduction reaction†

Hongyu Guo,^{‡a} Jamie A. Trindell,^{‡ab} Hao Li,^{‡abc} Desiree Fernandez,^a Simon M. Humphrey,^{‡a} Graeme Henkelman^{‡*abc} and Richard M. Crooks^{‡*ab}

In this report, density functional theory (DFT) calculations of O and OH binding energies on triatomic surface ensembles of Pd_xIr_(100-x) nanoalloys successfully predicted the overall trend in experimental oxygen reduction reaction (ORR) activity as a function of nanoparticle (NP) composition. Specifically, triatomic Pd₃ ensembles were found to possess optimal O and OH binding energies and were predicted to be highly active sites for the ORR, rivaling that of Pt(111). However, DFT calculations suggest that the O binding energy increases at active sites containing Ir, thereby decreasing ORR activity. Pd_xIr_(100-x) nanoalloys were synthesized using a microwave-assisted method and their activity towards the ORR was tested using rotating disk voltammetry (RDV). As predicted, the bimetallic electrocatalysts exhibited worse catalytic activity than the Pd-only NPs. The strong qualitative correlation between the theoretical and experimental results demonstrates that the activity of individual active sites on the surface of NPs can serve as a proxy for overall activity. This is a particularly useful strategy for applying DFT calculations to electrocatalysts that are too large for true first-principle analysis.

Received 15th December 2019
Accepted 5th April 2020

DOI: 10.1039/c9ta13711d

rsc.li/materials-a

Introduction

The use of density functional theory (DFT) calculations to accurately predict the electrocatalytic activity of metal nanoparticles (NPs) has previously been reported by our group¹⁻⁵ and many others.⁶⁻¹⁰ Most such studies focus exclusively on discovering compositions that are particularly effective electrocatalysts, but in the present report we demonstrate the power of DFT to also predict ineffective catalyst compositions. Significantly, we show that DFT-based catalytic modeling of small surface ensembles can accurately predict the catalytic activity of

nanoalloys having sizes too large for traditional DFT calculations.

Specifically, we performed DFT calculations on Pd_xIr_(100-x) alloy NPs and developed a theoretical model which predicted that alloying Ir into Pd should decrease the overall oxygen reduction reaction (ORR) activity of the Pd-based electrocatalyst. The calculations revealed that formation of Ir-containing surface ensembles was responsible for this behavior. To verify the theoretical predictions, we prepared different compositions of Pd_xIr_(100-x) nanoalloys using a microwave-radiation synthetic method. Subsequent electrochemical analysis confirmed the decrease in ORR activity of the nanoalloys as a function of increasing Ir content (and hence fewer Pd-rich ensembles on the surface).

ORR catalysts are often designed by taking advantage of the predictive power of a volcano plot,^{11,12} as previously developed by Nørskov and coworkers¹³ according to the Sabatier principle.¹⁴ For example, a 3D volcano plot for the ORR correlates the theoretical activity of an ORR catalyst with the calculated O and OH binding energies on metal surfaces.¹³ In the case of alloys, these binding energies can be influenced by ensemble, ligand, and strain effects, and therefore the resulting overall ORR activity does not always correlate linearly with composition.¹ By considering each of the foregoing factors, we recently found that the local electronic environment of reactive three-fold triatomic surface ensembles is often the main consideration controlling the O and OH binding energies on close-packed alloy surfaces.^{15,16} For example, we reported that

^aDepartment of Chemistry, The University of Texas at Austin, 105 E. 24th Street, Stop A5300, Austin, Texas 78712-1224, USA. E-mail: crooks@cm.utexas.edu; henkelman@utexas.edu; smh@cm.utexas.edu; Tel: +1-512-475-8674; +1-512-471-4179; +1-512-471-0312

^bTexas Materials Institute, The University of Texas at Austin, 105 E. 24th Street, Stop A5300, Austin, Texas 78712-1224, USA

^cThe Oden Institute for Computational Engineering and Sciences, The University of Texas at Austin, 105 E. 24th Street, Stop A5300, Austin, Texas 78712-1224, USA

† Electronic supplementary information (ESI) available: Plot of O and OH binding energies of triatomic surface ensembles on randomly alloyed Pd₈₀Ir₂₀(111); high-resolution XPS spectra for Pd_xIr_(100-x) NPs; PXRD analysis of Pd_xIr_(100-x) NPs; mass-loading (wt%) of each as-synthesized catalyst on Vulcan carbon; limiting CVs obtained for Pd_xIr_(100-x) NPs before and after ORR experiments; STEM images of the metal NPs used in this study after electrochemical ORR experiments; lattice constants for Pd_xIr_(100-x) NPs determined *via* PXRD. See DOI: 10.1039/c9ta13711d

‡ These authors contributed equally.

calculations of these binding energies on triatomic $\text{Rh}_x\text{Au}_{(3-x)}$ surface ensembles (*i.e.*, Au_3 , Rh_1Au_2 , Rh_2Au_1 , or Rh_3) accurately predicted the composition-dependent ORR performance of $\text{Rh}_x\text{Au}_{(100-x)}$ nanoalloys.¹⁷ In this case the Rh_1Au_2 alloy exhibited maximum activity.

Other research groups have reported similar composition-dependent ORR activities for nanoalloys.^{18–22} For example, Pd-based electrocatalysts such as PdCo ^{19,23–25} and PdFe ^{19,26–28} have been explored as promising ORR catalysts, with Pd_3M ($\text{M} = \text{Fe}$ or Co) structures reported to be particularly active. Unfortunately, these nanoalloys are of limited practical value as ORR catalysts due to electrochemical dissolution of the less noble atoms,²⁹ which leads to gradual loss of catalytic activity. One exception is PdIr alloys, where the high relative stability of Ir in acidic media is predicted to reduce overall metal dissolution, or leaching, from the catalysts. For example, PdIr dendritic nanostructures are stable under acidic conditions and they are active for the ORR.^{30–32} However, the structural complexity of nanodendrites makes it difficult to predict the relationship between their surface composition and ORR activity. Therefore, despite promising experimental results, challenges in both the synthesis and stability of well-defined Pd-alloy catalysts have limited the usefulness of theoretical tools in understanding and predicting their ORR activity.

In the present study, we carried out a DFT analysis of $\text{Pd}_x\text{Ir}_{(100-x)}$ NPs and found that Pd-only triatomic ensembles (Pd_3) on the surfaces of these nanoalloys should be the most active sites for the ORR in acidic media due to their optimal binding energies for reactive O and OH species. For fully random $\text{Pd}_x\text{Ir}_{(100-x)}$ NPs, the number of Pd_3 surface ensembles decreases as the percentage of Ir diluent atoms increases. This in turn is predicted to reduce ORR activity. To test this theoretical finding, we synthesized well-defined, highly faceted $\text{Pd}_x\text{Ir}_{(100-x)}$ NPs using a microwave radiation-assisted method.^{17,33–35} Specifically, $\text{Pd}_{75}\text{Ir}_{25}$, $\text{Pd}_{63}\text{Ir}_{37}$, and $\text{Pd}_{50}\text{Ir}_{50}$, as well as Pd-only and Ir-only NPs, were prepared. Subsequent experimental electrochemical measurements in acidic media confirmed the theoretical predictions.

Experimental section

Chemicals

All chemicals were used as received unless otherwise noted. IrCl_3 (99.9%) was obtained from Strem Chemicals (Newburyport, MA) and K_2PdCl_4 (min 32% Pd) was purchased from Acros Organics (Fair Lawn, NJ). Poly(vinylpyrrolidone) (PVP, $\langle \text{MW} \rangle = 58\,000$) was obtained from Alfa Aesar (Ward Hill, MA). HClO_4 (70 wt%, reagent ACS grade), HCl (37 wt%, trace metal grade), H_2O_2 (30 wt%, certified ACS grade), ethylene glycol (certified grade) and 2-propanol (certified ACS plus) were purchased from Fisher Scientific (Fair Lawn, NJ). Vulcan carbon (XC-72R), used to prepare the catalyst inks, was from Fuel Cell Store (College Station, TX). Nafion 117 solution (5 wt% in MeOH) was purchased from Sigma-Aldrich (St. Louis, MO). Gases, including O_2 (99.999%, research grade) and Ar (99.99%), were purchased from Praxair, Inc. (Austin, TX). Nylon membrane filters (0.22 μm pore size) were purchased from

Simsii, Inc. (Irvine, CA). Unless otherwise indicated, all aqueous solutions were prepared using deionized (DI) water (18.2 $\text{M}\Omega$ cm Milli-Q water, Millipore, Bedford, MA).

Computational methods

All DFT calculations were performed using the Vienna *ab initio* Simulation Package code. Core electrons were described by a projector augmented-wave method.³⁶ Electronic exchange and correlation were described by the generalized gradient approximation with a Perdew–Burke–Ernzerhof functional.³⁷ Kohn–Sham wave functions, expanded in a plane wave basis, were used to describe the valence electrons.³⁸ Standard potentials were used to describe the core electrons. The Brillouin zone was sampled through a $3 \times 3 \times 1$ Monkhorst–Pack k -point mesh.³⁹ The energy cutoff for the calculations was set at 400 eV with a force convergence criterion of 0.05 eV \AA^{-1} on each atom. The total energies of O_2 and OH in vacuum were calculated with spin-polarization. The zero-point energy and entropic correction values were obtained from Nørskov *et al.*¹³ and applied at 298 K. A charge analysis using the Bader method was performed to study the electron charge transfer of the surface elements.⁴⁰

Modeling methods

All surfaces in this study were modeled as (111) slabs with (4×4) unit cells and four layers, with the lattice constants calculated from Vegard's law.⁴¹ A vacuum layer of at least 10 \AA was used to separate the surfaces from their images in the z -direction. The bottom two layers were constrained in bulk positions, while the topmost two layers were able to relax freely. Thicker slabs were tested in our previous studies on Pd-alloys;⁴² no significant change was observed on the calculated binding energies. Initial theoretical calculations for ensemble binding energies were performed using a slab model with a nominal composition of $\text{Pd}_{50}\text{Ir}_{50}$. For the $\text{Pd}_{50}\text{Ir}_{50}(111)$ alloy model surface,¹⁵ nine randomly alloyed slabs were generated based on the Atomic Simulation Environment library.⁴³ The lattice constant of the $\text{Pd}_{50}\text{Ir}_{50}(111)$ random-alloy models was calculated to be 3.86 \AA . We note that the sampling method for alloys results in configurations with both relatively low and high surface energies, which is expected to be representative for the synthesis of classically immiscible bimetallic alloys using kinetically-controlled methods. The relatively small deviation of adsorbate binding energies (as discussed later) indicates that surface energy is not a significant factor affecting the adsorbate binding strength. The $\text{Pd}_1\text{Ir}_2/\text{Ir}(111)$, $\text{Pd}_2\text{Ir}_1/\text{Ir}(111)$, and $\text{Pd}_3/\text{Ir}(111)$ ensembles were modeled as the Ir(111) substrate replaced by one, two (2-fold), and three (3-fold) Pd atoms on the surface, respectively.

Modeling of the volcano activity plot for the ORR is based on the micro-kinetic modeling developed by Nørskov *et al.*;¹³ complete details can be found in a previous paper from our groups.¹⁷ The binding energies of O (E_{OB}) and OH (E_{OHB}) were calculated using eqn (1) and (2), respectively.

$$E_{\text{OB}} = E_{\text{tot}} - E_{\text{Slab}} - \frac{1}{2}E_{\text{O}_2} \quad (1)$$

$$E_{\text{OHB}} = E_{\text{tot}} - E_{\text{Slab}} - E_{\text{OH}} \quad (2)$$

Here, E_{tot} is the total energy of the adsorption system, E_{Slab} is the total energy of a bare slab, E_{O_2} is the total energy of O_2 in vacuum, and E_{OH} is the total energy of OH in vacuum.

The overall theoretical ORR activity of the synthesized $\text{Pd}_x\text{Ir}_{(100-x)}$ NPs was modeled using a similar method,³³ which included the NP size, alloy ensemble composition, and the ensemble activity. The total number of atoms for each composition of $\text{Pd}_x\text{Ir}_{(100-x)}$ NP was estimated using the closest magic number for a cubooctahedral NP of the average size as determined by TEM.⁴⁴ The nanoalloy compositions, obtained using inductively coupled plasma-optical emission spectroscopy (ICP-OES), were used as the alloy composition in the model. The distributions of alloyed surface ensembles were calculated with the assumption that the Pd and Ir are distributed randomly on the surface (eqn (3)–(6)).

$$D_{\text{Pd}_3} = \text{Pd}\% ^3 \quad (3)$$

$$D_{\text{Pd}_2\text{Ir}_1} = 3\text{Pd}\% ^2(1 - \text{Pd}\%) \quad (4)$$

$$D_{\text{Pd}_1\text{Ir}_2} = 3\text{Pd}\%(1 - \text{Pd}\%)^2 \quad (5)$$

$$D_{\text{Ir}_3} = (1 - \text{Pd}\%)^3 \quad (6)$$

In the foregoing equations, Pd% represents the composition of Pd determined by ICP-OES, D_{Pd_3} , $D_{\text{Pd}_2\text{Ir}_1}$, $D_{\text{Pd}_1\text{Ir}_2}$, and D_{Ir_3} represent the distributions of the 3-fold triatomic ensembles Pd_3 , Pd_2Ir_1 , Pd_1Ir_2 , and Ir_3 , respectively. The theoretical activities of each ensemble were estimated using their average O and OH binding energies and the previously developed microkinetic model.^{13,17} Using the NP size, ensemble composition, and ensemble activity, the theoretical activity (R) for each PdIr NP can be estimated using eqn (7).

$$R = \frac{N_{(111)}(D_{\text{Pd}_3}R_{\text{Pd}_3} + D_{\text{Pd}_2\text{Ir}_1}R_{\text{Pd}_2\text{Ir}_1} + D_{\text{Pd}_1\text{Ir}_2}R_{\text{Pd}_1\text{Ir}_2} + D_{\text{Ir}_3}R_{\text{Ir}_3})}{N_{\text{tot}}} \quad (7)$$

Here, $N_{(111)}$ represents the total number of atoms in the (111) surface, N_{tot} represents the total number of atoms in the NP (using the diameter determined from TEM), while R_{Pd_3} , $R_{\text{Pd}_2\text{Ir}_1}$, $R_{\text{Pd}_1\text{Ir}_2}$, and R_{Ir_3} represent the theoretical activity of the four triatomic ensembles estimated from their O and OH binding energies. Because the ensemble effect is found to predominate over electronic and strain effects on alloy surfaces,¹⁵ different compositions of PdIr alloys do not lead to significant changes in the average binding energies at each ensemble.

Synthesis of PVP-capped $\text{Pd}_x\text{Ir}_{(100-x)}$ NPs

$\text{Pd}_x\text{Ir}_{(100-x)}$ NPs were prepared using a modified polyol method.⁴⁵ Taking $\text{Pd}_{50}\text{Ir}_{50}$ NPs as an example, PVP (50.0 mg, 0.45 mmol) was pre-dissolved in 15.0 mL of ethylene glycol (EG) contained in a flask fitted with a cold-water reflux. The apparatus was transferred to a CEM MARS-5 microwave reactor and preheated to 150 °C with continuous stirring (450 rpm). A

solution containing $\text{IrCl}_3 \cdot n\text{H}_2\text{O}$ (14.9 mg, 0.05 mmol) and $\text{K}_2\text{-PdCl}_4 \cdot n\text{H}_2\text{O}$ (16.3 mg, 0.05 mmol) in 5.0 mL of EG was then added at a rate of 300 mL h^{-1} (controlled by a syringe pump). For $\text{Pd}_x\text{Ir}_{(100-x)}$ NPs of varying compositions, the weights and ratios of the metal precursors was modified while the total concentration of the two metals (Pd + Ir) was kept at 20 mM. After addition, the mixture was kept at 150 °C for another 30 min, and then the reaction was quenched by placing the flask into an ice-water bath. The resulting NPs were precipitated from solution by addition of excess acetone and then collected by centrifugation. Finally, the NPs were washed twice with ethanol and then dried under vacuum prior to characterization.

The $\text{Pd}_x\text{Ir}_{(100-x)}$ NPs were immobilized on carbon ($\text{Pd}_x\text{Ir}_{(100-x)}/\text{C}$) as follows: 2.5 mg of the NPs were dispersed in 45 mL of EG, and the resulting solution was added dropwise to a dispersion of 47.5 mg Vulcan carbon in 250 mL EtOH. The target loading of the catalyst was 5 wt%. The mixture was stirred for 24 h and the resulting catalyst ink was collected by vacuum filtration over a nylon membrane and dried under vacuum.

Physical characterization of $\text{Pd}_x\text{Ir}_{(100-x)}$ NPs

Powder X-ray diffraction (PXRD) patterns of $\text{Pd}_x\text{Ir}_{(100-x)}$ NPs were collected using a Rigaku R-Axis Spider Diffractometer having a Cu source operating at 1.6 kW. ICP-OES analysis was performed using a Varian 710-ES spectrometer. The samples were prepared by digesting the $\text{Pd}_x\text{Ir}_{(100-x)}$ NPs (or $\text{Pd}_x\text{Ir}_{(100-x)}/\text{C}$) in a mixture of HCl and H_2O_2 (3/1 v/v) in a CEM-MARS-5 microwave reactor at 200 °C for 2 h.

X-ray photoelectron spectroscopy (XPS) was carried out using a Kratos X-ray photoelectron spectrometer having a monochromatic Al- K_{α} source. Samples for XPS analysis were prepared by drop-casting NPs dispersed in EtOH onto indium-tin oxide (ITO)-coated glass slides.

Transmission electron microscopy (TEM) images of the as-synthesized NPs were collected using a FEI Tecnai instrument operating at 80 kV. Samples were prepared by drop-casting 10 μL ethanolic suspensions of NPs onto Formvar-coated Cu grids (Ted Pella, Inc., Redding, CA).

Electrode preparation

Approximately 4 mg of each $\text{Pd}_x\text{Ir}_{(100-x)}/\text{C}$ composite ink were reconstituted *via* sonication in 400 μL of 2-propanol and 20 μL of 5 wt% Nafion 117 solution for ~ 5 min. 2.0 mL of DI water was then added to the mixture, followed by an additional ~ 15 min of sonication to yield a homogenous ink solution. Catalyst-coated electrodes were prepared by drop-casting 20 μL of ink (5 μL at a time) onto a 3 mm glassy carbon rotating disk electrode (GC-RDE) and drying the ink under a gentle flow of Ar gas. Between each set of electrochemical experiments, the working electrode was polished using 0.3 μm alumina (Buehler, Lake Bluff, IL).

Electrochemical measurements

Electrochemical measurements were obtained using either a CH Instruments Model CHI650C or CHI700D Electrochemical Analyzer (Austin, TX) and a single-compartment, three-electrode electrochemical cell. Electrochemical potentials were measured

vs. an Hg/Hg₂SO₄/saturated K₂SO₄ (CH Instruments, Inc.) reference electrode, and then converted to the reversible hydrogen electrode (RHE) potential using the measured pH value of 1.0 for the 0.10 M HClO₄ electrolyte solution. A glassy carbon rod (100 mm long, 6 mm in diameter, Alfa Aesar, Tewksbury, MA) was used as the counter electrode. Electrochemical cleaning scans were first collected in 12 mL of Ar-saturated, 0.10 M HClO₄ by cycling the electrode potential from 0.30 V to 1.50 V and then back to 0.30 V (vs. RHE) at a scan rate of 50 mV s⁻¹. A total of 14 cleaning scans were collected, by which time the cyclic voltammograms (CVs) attained limiting behavior.

The ORR experiments were carried out using a Metrohm Autolab RDE and motor control unit. The ORR scans were collected in 12 mL of O₂-saturated, 0.10 M HClO₄ using linear sweep voltammetry (LSV) starting at 1.10 V and ending at 0.40 V (vs. RHE). The scan rate was 20 mV s⁻¹ and the rotation rate was 1600 rpm. Next, background LSVs were collected using the parameters noted for the ORR measurements, but in Ar-saturated, 0.10 M HClO₄. Following these LSVs, two CVs were collected using the experimental parameters noted for the electrochemical cleaning scans. This precaution was taken to confirm that those CVs did not change after electrocatalytic measurements, thereby ensuring the level of stability of the catalyst during ORR.

Post-characterization of catalytic inks

Scanning transmission electron microscopy (STEM) and energy dispersive spectroscopy (EDS) were used to analyze the size and composition of the Pd_xIr_(100-x)/C inks after electrochemical experiments. The resulting sizes and compositions were used in the theoretical calculations to ensure the active catalytic structures were modeled. These studies were carried out using a JEOL 2010F transmission electron microscope having a point-to-point resolution of 0.19 nm and an accelerating voltage of 200 kV. TEM grids of the catalyst inks (after electrocatalysis) were prepared by wiping a lacey carbon-coated Cu grid (Electron Microscopy Sciences, Hatfield, PA) across the electrode surface. Size distributions were determined by analyzing 200 particles from three independent electrocatalytic experiments. Consequently, a total of 600 particles were analyzed after electrocatalysis.

Results and discussion

Computational predictions for the ORR activity of Pd_xIr_(100-x) NPs

To theoretically predict the electrocatalytic ORR activity of Pd_xIr_(100-x) NPs, the O and OH binding energies were calculated and plotted as a function of ensemble composition. Fig. 1a shows that on alloyed Pd₅₀Ir₅₀ surfaces, the O binding energies of the triatomic ensembles become monotonically stronger (*i.e.*, more negative) with increasing Ir-content; the Ir₃ surface site has the strongest O binding energy. Interestingly, this same trend is not observed for the calculated OH binding energies, as shown in Fig. 1b. In this case, Ir₃ displays more favorable (*i.e.*, weaker) OH binding compared to the Pd₂Ir₁ and Pd₁Ir₂ surface ensembles. This difference between O and OH binding energy trends on PdIr surface ensembles is significant, because it suggests that the well-

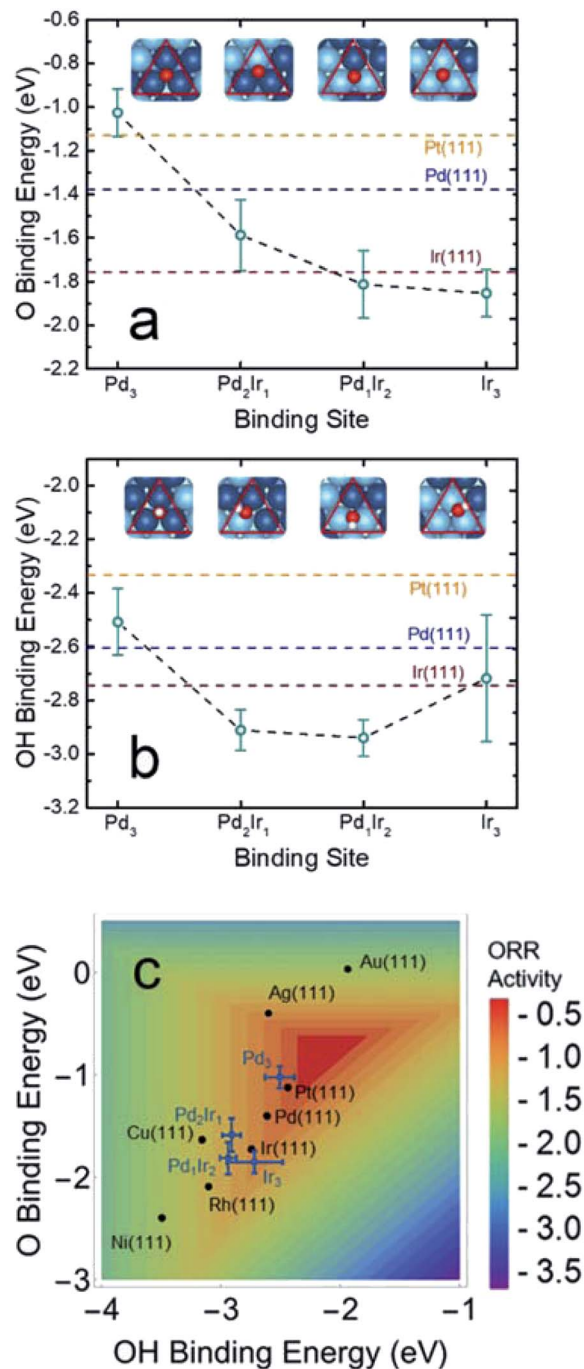


Fig. 1 Plots of the calculated (a) O and (b) OH binding energies for the four different triatomic ensembles of PdIr on randomly alloyed Pd₅₀Ir₅₀(111) model. The red, blue, and orange dashed lines represent the binding energies on Ir, Pd, and Pt(111), respectively. Each error bar was calculated using ten sampled binding sites on nine randomly alloyed Pd₅₀Ir₅₀(111) surfaces. Insets show the representative optimized binding geometries of O and OH. Blue, light blue, red, and white spheres represent Pd, Ir, O, and H, respectively. (c) Volcano plot of ORR activity on monometallic (111) surfaces (black marks) and PdIr alloyed triatomic ensembles on randomly alloyed Pd₅₀Ir₅₀(111) surfaces (blue marks).

known scaling relationship between O and OH bindings can be broken on Pd_xIr_(100-x) random alloys.⁴⁶ These randomly alloyed models were also compared with intermetallic alloy structures

(Table S1[†]); no significant deviations were found in the trends of the calculated O and OH binding energies.

Finally, the 3D volcano plot in Fig. 1c correlates both the O and OH binding energies of the surface ensembles with their predicted ORR activities. Significantly, this plot shows that the Pd₃ triatomic ensemble lies close to the volcano peak. This indicates a high theoretical ORR activity, rivaling even that of Pt(111).

Notably, all of the surface ensemble activity trends shown in Fig. 1 were calculated using a Pd₅₀Ir₅₀(111) random alloy model. The assumption that the same triatomic ensembles should possess similar O and OH binding energies on all Pd_xIr_(100-x) compositions is based on our recent studies of other Pd-based alloys.¹⁵ To test the validity of using the surface ensemble binding energies calculated for a Pd₅₀Ir₅₀ model to predict the overall activities of other Pd_xIr_(100-x) compositions, additional DFT calculations were performed on a Pd₈₀Ir₂₀(111) model. Specifically, the data shown in Fig. 1a and b was recalculated by considering the O and OH binding energies on surface ensembles of a Pd₈₀Ir₂₀ random alloy, and the results are shown in Fig. S1 in the ESI.[†] The overall trends in O and OH binding energies on Pd₈₀Ir₂₀ surfaces are similar to those calculated for Pd₅₀Ir₅₀. Because adsorbate bindings at surface ensembles are independent of the alloy composition,¹⁵ the reactivity of the Pd₃ ensembles is not expected to be significantly different on Ir-rich Pd_xIr_{100-x} alloys. Taken together, these results suggest that regardless of the overall alloy composition, maximizing the number of Pd₃ surface sites can improve ORR activity, whereas ensembles containing Ir decrease ORR activity.

Mechanistic insights into the alloying effect

While Pd-only ensembles possess the highest activities, as discussed in the previous section, the presence of Ir can further optimize the reactivity of these Pd₃ sites. To provide mechanistic insights into the effect of alloying in Pd_xIr_(100-x) NPs, the reaction free energies of the ORR, proceeding *via* a dissociative mechanism, were calculated using a previously reported method.¹³ Specifically, we evaluated the electronic contribution of Ir to Pd by using flat-surface alloy models of Pd_x ($x = 1, 2,$ and 3) ensembles doped into an Ir(111) surface (modeling details can be found in the Experimental section). The optimized adsorption configurations for the ORR intermediates on these surfaces are provided in Fig. S2.[†] On the basis of the resulting free energy diagrams, plotted in Fig. 2a, the Pd₃ ensemble [Pd₃/Ir(111)] (a 3-fold Pd-trimer doped into an Ir(111) surface) should out-perform Pd(111), Ir(111), and other PdIr/Ir(111) surfaces. Specifically, these results predict that the presence of Ir in the NP will lead to better activity at the Pd₃ ensembles due to electronic and strain effects. However, alloying Ir into Pd could significantly reduce the number of highly active Pd₃ surface sites, leading to lower overall activity of the catalyst. Accordingly, the balance between these two factors will strongly affect the ORR activity.

To qualitatively understand the site-specific reactivity discussed above, the average energies of the d-electrons (*i.e.*, d-band centers) were calculated on the triatomic ensembles on Ir(111) doped with different ratios of Pd, reasoning that these

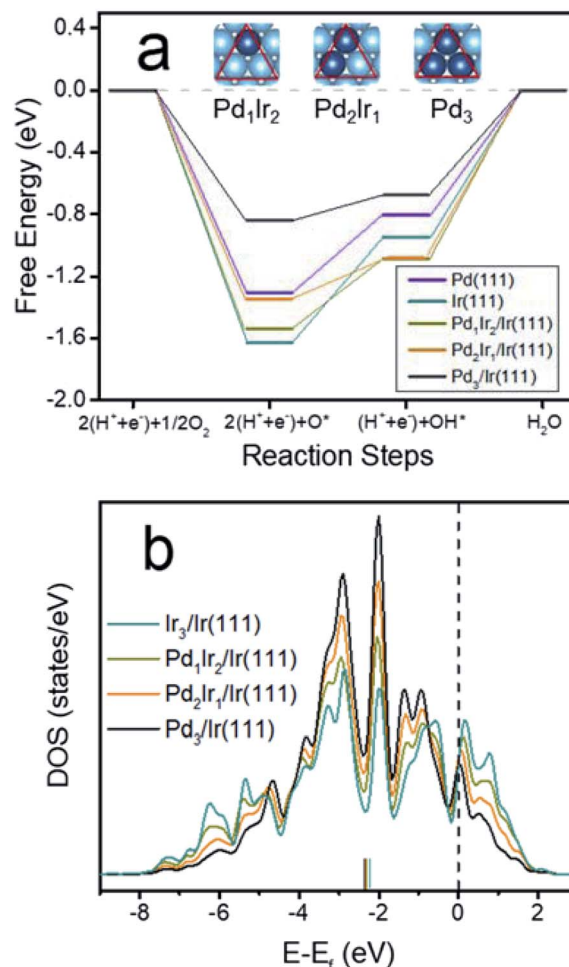


Fig. 2 (a) Free energy diagram for the ORR and (b) calculated projected density of states (PDOS) for d-electrons of Pd_xIr_(3-x)/Ir(111), Pd(111), and Ir(111) surfaces. The Pd₁Ir₂/Ir(111), Pd₂Ir₁/Ir(111), and Pd₃/Ir(111) were modeled as the Ir(111) substrate replaced by 1, 2 (2-fold), and 3 (3-fold) Pd atoms on the surface, respectively. Insets show the geometries of the Pd_xIr_(3-x) ensembles considered for these calculations. Blue and light blue spheres represent Pd and Ir, respectively. The calculated d-band center values are -2.32 , -2.34 , -2.35 , and -2.36 eV, for Ir₃, Pd₁Ir₂, Pd₂Ir₁, and Pd₃, respectively.

ensemble effects are less explored in previous studies as compared to the widely studied Pd(111) surface. Fig. 2b shows the calculated projected density of states (PDOS) of the d-electrons of all possible PdIr triatomic surface ensembles on an Ir(111) surface. The calculated d-band centers slightly downshift with a decreasing number of Ir atoms in the triatomic ensemble. This is due to a combination of ensemble, electronic, and strain effects. Each individual effect should lead to a specific tuning direction of the binding energies, but the d-band center includes all three of these effects. On the basis of the principles of d-band center theory,⁴⁷ this down shift of the d-band center upon alloying of Ir and Pd is likely responsible for the optimal binding energies of O and OH over Pd₃ ensembles as indicated by the ORR volcano (Fig. 1c).

As tabulated in Table S2,[†] alloying Pd with Ir generally lengthens the surface bonds due to the larger lattice constant

of Pd. It also, however, leads to an electron charge gain of the surface Ir sites, which in turn increases the filling of the Ir local d-band and down-shifts the d-band center. Given that Ir(111) binds adsorbates more strongly than Pd(111) (Fig. 1), the tuning of adsorbate binding energies is predominately due to an Ir electronic effect. Interestingly, the shape of the d-band of Pd₃/Ir(111) is significantly different from that of Pd₃/Pd(111) (Fig. S3†). This observation indicates that, in addition to the d-band center, the d-band shape also impacts the adsorbate binding energies when the PDOS of the two surfaces are significantly different.⁴⁸ All these effects lead to optimized, site-specific ORR activity on these pure Pd ensembles.

Synthesis and characterization of Pd_xIr_(100-x) NPs

The method used for synthesizing Pd_xIr_(100-x) NPs is described in detail in the Experimental section. Briefly, a solution of PVP in ethylene glycol was heated inside a CEM microwave reactor prior to the addition of a solution containing hydrated IrCl₃ and K₂PdCl₄ salts, at a rate of 6.0 mmol_{Pd+Ir} h⁻¹. The metal precursor solution was initially yellow but quickly turned black upon addition to the heated reaction solution, indicating fast co-reduction of Pd²⁺ and Ir³⁺ by ethylene glycol. A wide compositional range of Pd_xIr_(100-x) NPs could be conveniently obtained by changing the ratio of metal precursors (*i.e.*, Pd²⁺ : Ir³⁺). For this study, we focused on just three different alloys having the nominal compositions: Pd₅₀Ir₅₀, Pd₆₃Ir₃₇, and Pd₇₅Ir₂₅. Additionally, both Pd-only and Ir-only NPs were prepared using the same method, except with the addition of only K₂PdCl₄ or IrCl₃ precursors, respectively.

ICP-OES was used to determine the actual resulting compositions of the Pd_xIr_(100-x) NPs, and the values obtained were in close agreement to the molar ratios of K₂PdCl₄ to IrCl₃ used for the synthesis (Table 1). The ICP-OES data were taken as the actual alloy compositions of the as-synthesized NPs, and therefore these materials will henceforth be referred to as Pd₇₄Ir₂₆, Pd₆₃Ir₃₇, and Pd₄₉Ir₅₁.

XPS analysis indicated that the NPs were mostly metallic with a slight amount of oxidation. Specifically, the Ir 4f binding energies of the Pd_xIr_(100-x) NPs undergo a small negative shift relative to Ir-only NPs, changing from 60.8 eV to 60.5 eV (Fig. S4a†). In contrast, the Pd 3d binding energies shift positive relative to pure Pd NPs, changing from 334.9 eV to 335.1 eV (Fig. S4b†). These shifts in binding energy as a function of alloy composition are indicative of charge transfer from Pd to Ir.⁴⁹⁻⁵¹

The powder X-ray diffraction data (Fig. S5a†) for the as-synthesized Pd_xIr_(100-x) NPs indicate that they exhibit a face-centered cubic (fcc) structure. A consistent shift of the diffraction peaks to higher angles is observed at higher Ir content, because Ir has a smaller lattice constant than Pd. It is also worth noting that Pd_xIr_(100-x) NPs with higher Ir-compositions exhibit broader diffraction peaks, indicating a smaller particle size than those containing less Ir. The pure Ir NPs are so small that some pairs of diffraction peaks, for example, the (111) and (200), as well as (311) and (222), overlap, thereby limiting the usefulness of this technique for these materials.^{52,53}

Table 1 Pd and Ir compositions of the Pd_xIr_(100-x) NP catalysts

Nominal ratios employed during synthesis ^a		ICP-OES analysis of NPs prior to catalysis ^b		STEM-EDS data for NPs after catalysis ^c	
% Pd	% Ir	% Pd	% Ir	% Pd	% Ir
75	25	73.7 ± 0.9	26.3 ± 0.9	83 ± 5	17 ± 5
62	38	63.0 ± 0.8	37.0 ± 0.8	76 ± 10	24 ± 10
50	50	48.9 ± 0.9	51.1 ± 0.9	56 ± 16	44 ± 16

^a Nominal compositions, which reflect the percentages of the precursors used for the synthesis. ^b The as-synthesized Pd : Ir ratios determined using ICP-OES were obtained from three independent analyses using freshly synthesized NPs and are used as the actual compositions of the alloys. ^c The Pd : Ir ratios determined from STEM-EDS reflect measurements obtained from ten individual NPs following three independent ORR experiments (for a total of thirty NPs analyzed for each Pd_xIr_(100-x) composition). The compositional data from STEM-EDS were used for the final theoretical calculations.

The (111) *d*-spacings of Pd_xIr_(100-x) NPs, derived from Vegard's law,⁴¹ display a linear relationship with composition (Fig. S5b†), suggesting random alloy structures were obtained regardless of Pd : Ir composition. Finally, from the PXRD results, the measured lattice constant of the Pd NPs is 3.91 Å (Table S3†). For comparison, the known lattice constant for bulk Pd is 3.89 Å.⁵⁴ The good agreement in lattice constant between the Pd NPs and bulk Pd indicates that NP strain effects are negligible in the present system. Accordingly, no additional strain effects were considered during modeling.

Transmission electron microscopy (TEM) was used to characterize the average size of the Pd_xIr_(100-x) NPs. Fig. 3a is a representative TEM image for Pd₄₉Ir₅₁ NPs, and Fig. 3b shows the corresponding average size-distributions as a function of Pd-content. All of the Pd-containing catalysts exhibit similar average sizes, while the Ir-only NPs had diameters of just 1.7 ± 0.3 nm. Energy dispersive spectroscopy (EDS) mapping was used to determine the compositional distribution of the nanoalloys. Fig. 3c-f display representative EDS data for Pd₄₉Ir₅₁ NPs. Pd and Ir are evenly distributed, suggesting an alloy structure as previously indicated by PXRD.

Electrocatalytic activity of Pd_xIr_(100-x) for the ORR

In preparation for electrochemical measurements, the NP catalysts were immobilized on Vulcan carbon (C) at an average metal loading of ~2 wt%, as determined by ICP-OES (Table S4†). The resulting conductive inks (Pd_xIr_(100-x)/C) were used to modify glassy carbon working electrodes. Prior to the ORR studies, CV was used to remove the PVP-capping ligands and to increase the electrocatalytically active surface area of the NPs. These cleaning scans were conducted in Ar-saturated, 0.10 M HClO₄ by cycling the electrode potential ten times (or until the CVs attained limiting behavior) between 0.15 V and 1.50 V (all potentials are *vs.* RHE) at 50.0 mV s⁻¹.

Fig. 4a shows the steady-state, limiting CVs for each of the Pd_xIr_(100-x)/C-modified electrodes. The CV of the Pd-only NPs

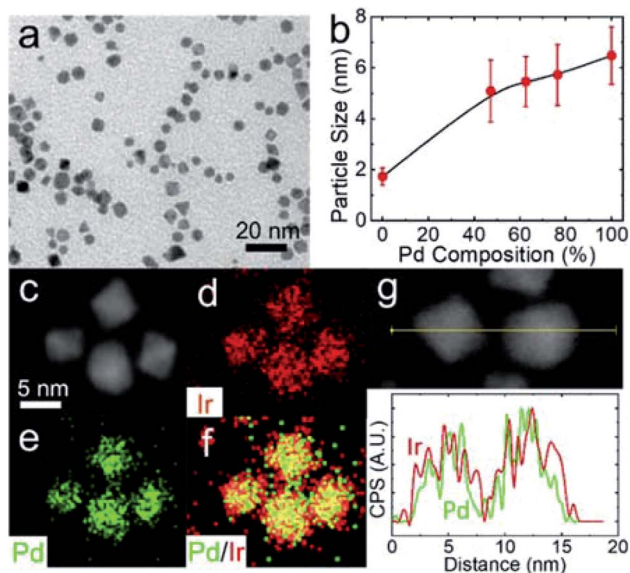


Fig. 3 TEM and EDS results for Pd₄₉Ir₅₁ NPs. (a) TEM image for Pd₄₉Ir₅₁ NPs. (b) Plot showing NP size distributions as a function of Pd composition (%) (c) HAADF-STEM image of four Pd₄₉Ir₅₁ NPs with EDS mapping of the NPs for (d) Ir; (e) Pd; and (f) an overlay of Pd and Ir. (g) Line-scan profile of two NPs with corresponding element signal count.

(Pd/C) exhibits two principal features: (1) reduction of surface PdO_x at ~0.7 V and (2) smaller hydride adsorption/desorption peaks between ~0.40 V and 0.15 V. These features are consistent with previous reports.^{55–57} In contrast, the CV for the Ir-only catalyst (Ir/C) is essentially featureless. The CVs for the mixed Pd_xIr_(100–x)/C alloy-modified electrodes exhibit intermediate behavior between these two extremes, as exemplified by the proportional decrease in the PdO_x reduction peak with decreasing mole fraction of Pd. In fact, integration of the PdO_x peaks indicates that the average percentages of Pd on the NP surfaces are 78 ± 2%, 57 ± 7%, and 44 ± 3% for Pd₇₄Ir₂₆ (73.7 ± 0.9%), Pd₆₃Ir₃₇ (63.0 ± 0.8%), and Pd₄₉Ir₅₁ (48.9 ± 0.9%), respectively, where the percentages in parentheses correspond to the overall percentages of Pd determined by ICP-OES. This degree of agreement suggests that these NPs are random alloys, which have surface compositions that reflect their bulk compositions.

Fig. 4b compares rotating disk voltammograms (RDVs) for each of the Pd_xIr_(100–x)/C-modified electrodes during ORR electrocatalysis. Specifically, these scans were obtained in O₂-saturated, 0.10 M HClO₄ by scanning the electrode potential from 1.10 V to 0.40 V. There are two important outcomes from these experiments. First, the limiting currents (*i*_l) for the RDVs are about the same, indicating that the catalyst loadings are about the same for each of the five electrocatalysts. Second, the half-wave potentials (*E*_{1/2}) move progressively more negative as the Ir content of the NPs increases. These results are significant, because they clearly indicate that increasing Ir content leads to poorer electrocatalytic activity of the NPs. This, in turn, supports the theoretical finding that Ir-containing surface ensembles are less active for the ORR than Pd-only ensembles.

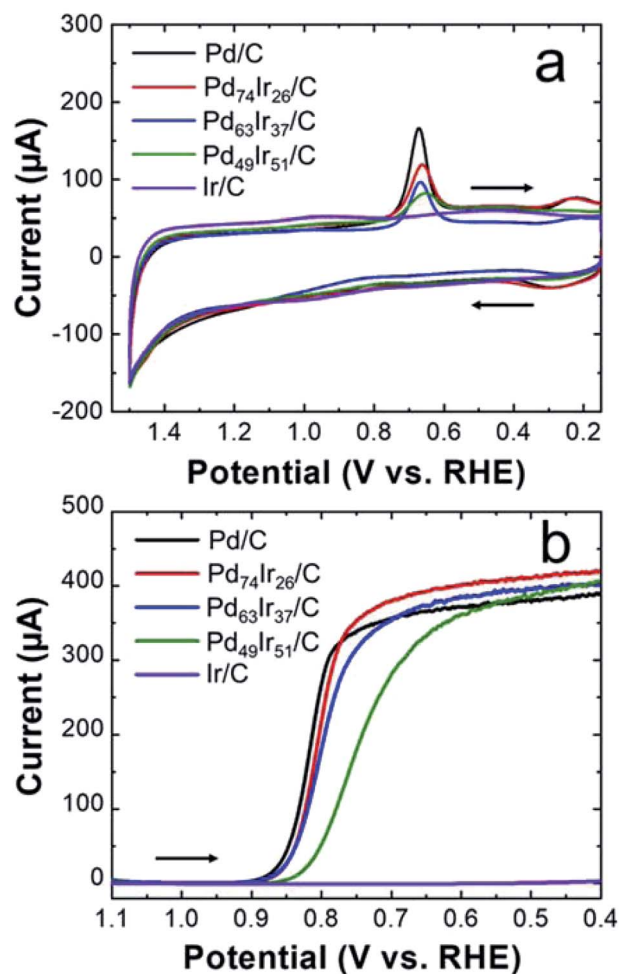


Fig. 4 (a) Cyclic voltammograms (CVs) of all catalysts upon completion of electrochemical cleaning scans. The CVs were collected in Ar-purged, 0.10 M HClO₄ by scanning the electrode potential from 0.15 V to 1.50 V (vs. RHE) at 50.0 mV s⁻¹. (b) Rotating disk voltammograms (RDVs) showing the activity of all catalysts towards the oxygen reduction reaction (ORR) in O₂-saturated, 0.10 M HClO₄. The scans commenced at 1.10 V and continued to 0.40 V (vs. RHE). The scan rate was 20.0 mV s⁻¹ and the rotation rate of the electrode was 1600 rpm. Arrows in both frames indicate the scan direction.

To probe the stability of the NPs, CVs were obtained after the ORR using the same procedure used to obtain the pre-ORR cleaning scans. The pre- and post-ORR CVs are compared in Fig. S6†. The near-overlap of these pairs of CVs confirms the stability of the NPs during the ORR. This is a somewhat surprising result, because Pd has previously been reported to exhibit poor stability in acidic media.⁵⁸

The NP sizes and compositions used for the theoretical calculations were obtained using STEM-EDS data obtained from catalyst inks collected from the working electrode after ORR experiments. Fig. S7† shows representative STEM images and overall size distributions of the catalytic inks after the ORR, and Table 1 provides the average NP compositions determined by EDS. In all cases there was a ~10% decrease in the total Ir content of individual NPs following the ORR.

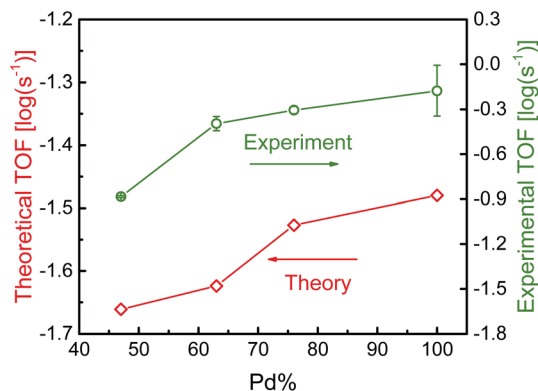


Fig. 5 Comparison of the theoretical and experimental TOFs as a function of the percentage of Pd in the NPs. The theoretical TOFs were calculated by considering the composition and size of NPs after catalysis. The alloy compositions used were those determined by EDS following the ORR (see Table 1).

As discussed in the Experimental section, eqn (3)–(7) were used to calculate the theoretical ORR activity as a function of Pd content. Specifically, the atomic numbers used in eqn (7) for Pd₄₉Ir₅₁, Pd₆₃Ir₃₇, Pd₇₄Ir₂₆, pure Pd, and pure Ir NPs were 6525, 5083, 8217, 6525, and 309, respectively (see details in the Experimental section). Fig. 5 compares the theoretically predicted ORR activities to those found experimentally. The qualitative agreement in the relative trends between the theoretical and experimental TOFs further supports the hypothesis that ensemble effects dominate the ORR activities of these Pd_xIr_(100-x) NPs. Due to the lack of experimental insight into O and OH surface adsorbate coverages, this theoretical model is not quantitatively informative and only the qualitative trends should be compared with the experimental data.^{16,59}

Summary and conclusions

In this report, the relative ORR activities of Pd_xIr_(100-x) NPs were evaluated using DFT analysis of triatomic surface ensembles. Specifically, the Pd₃ ensembles were predicted to possess favorable O and OH binding energies, resulting in ORR activity rivaling that of Pt(111). However, dilution of Pd on the NP surface occurs with increasing Ir-content, diminishing the number of Pd₃ active sites on the surface and decreasing the overall activity. Experimental RDV measurements confirm decreasing electrocatalytic ORR activity with increasing Ir-content, with the pure Pd/C catalyst showing maximum relative activity. This result is attributed to the presence of Ir-containing triatomic surface ensembles (*i.e.*, Pd₂Ir₁, Pd₁Ir₂, and Ir₃), which bind O too strongly, thereby deactivating the catalyst towards the ORR.

The strong qualitative correlation between the theoretical and experimental results (Fig. 5) demonstrates the power of theory for predicting the composition-dependent ORR activity of Pd_xIr_(100-x) NPs. Specifically, the observed ORR reactivity of Pd_xIr_(100-x) electrocatalysts changed as a function of overall surface ensemble activities, with compositional effects

dominating NP size and other alloying effects. This use of DFT calculations to understand catalyst reactivity is vital for designing increasingly active catalysts as standard first-principle DFT calculations are only applicable for NPs <~2 nm in diameter. By considering ensemble reactivities, however, it was possible to use DFT to successfully predict the ORR activities of larger NPs (*i.e.*, 5–7 nm) that have good qualitative agreement with experiment. This finding suggests that DFT calculations focusing on ensemble effects could be generally useful predictors for other types of catalysts.

Conflicts of interest

There are no conflicts to declare.

Acknowledgements

RMC and GH gratefully acknowledge support from the Chemical Sciences, Geosciences, and Biosciences Division, Office of Basic Energy Sciences, Office of Science, U.S. Department of Energy (Contract: DE-SC0010576); this grant supported the microscopy, XPS, and electrochemical analysis as well as the theoretical component of the work. SMH and GH acknowledge support from the National Science Foundation (Grant No: CHE-1807847); this grant supported the synthesis component as well as much of the NP characterization. We thank the Robert A. Welch Foundation (Grants: RMC, F-0032; GH, F-1841; SMH, F-1738) for sustained support of our research.

References

- 1 L. Luo, Z. Duan, H. Li, J. Kim, G. Henkelman and R. M. Crooks, *J. Am. Chem. Soc.*, 2017, **139**, 5538–5546.
- 2 L. Luo, L. Zhang, G. Henkelman and R. M. Crooks, *J. Phys. Chem. Lett.*, 2015, **6**, 2562–2568.
- 3 L. Luo, L. Zhang, Z. Duan, A. S. Lapp, G. Henkelman and R. M. Crooks, *ACS Nano*, 2016, **10**, 8760–8769.
- 4 R. M. Anderson, D. F. Yancey, L. Zhang, S. T. Chill, G. Henkelman and R. M. Crooks, *Acc. Chem. Res.*, 2015, **48**, 1351–1357.
- 5 D. F. Yancey, L. Zhang, R. M. Crooks and G. Henkelman, *Chem. Sci.*, 2012, **3**, 1033–1040.
- 6 L. Zhang, R. M. Anderson, R. M. Crooks and G. Henkelman, *Surf. Sci.*, 2015, **640**, 65–72.
- 7 J. Cho, I. Jang, H. S. Park, S. H. Choi, J. H. Jang, H. J. Kim, S. P. Yoon, S. J. Yoo and H. C. Ham, *Appl. Catal., B*, 2018, **235**, 177–185.
- 8 Y. Zhao, W. Zhang, H. Yin, J. He and Y. Ding, *Electrochim. Acta*, 2018, **274**, 9–15.
- 9 S. P. Lin, K. W. Wang, C. W. Liu, H. S. Chen and J. H. Wang, *J. Phys. Chem. C*, 2015, **119**, 15224–15231.
- 10 H. Ha, S. Yoon, K. An and H. Y. Kim, *ACS Catal.*, 2018, **8**, 11491–11501.
- 11 L. Zhang, R. Iyyamperumal, D. F. Yancey, R. M. Crooks and G. Henkelman, *ACS Nano*, 2013, **7**, 9168–9172.
- 12 W. Zhou, M. Li, O. L. Ding, S. H. Chan, L. Zhang and Y. Xue, *Int. J. Hydrogen Energy*, 2014, **39**, 6433–6442.

- 13 J. K. Nørskov, J. Rossmeisl, A. Logadottir, L. Lindqvist, J. R. Kitchin, T. Bligaard and H. Jónsson, *J. Phys. Chem. B*, 2004, **108**, 17886–17892.
- 14 T. Bligaard, F. Studt, A. J. Medford, A. Nilsson, J. S. Hummelshøj, F. Abild-Pedersen, A. Vojvodic, J. Voss and J. K. Nørskov, *J. Catal.*, 2015, **328**, 36–42.
- 15 H. Li, K. Shin and G. Henkelman, *J. Chem. Phys.*, 2018, **149**, 174705.
- 16 H. Li, E. J. Evans, C. B. Mullins and G. Henkelman, *J. Phys. Chem. C*, 2018, **122**, 22024–22032.
- 17 H. Li, L. Luo, P. Kunal, C. S. S. Bonifacio, Z. Duan, J. C. C. Yang, S. M. Humphrey, R. M. Crooks and G. Henkelman, *J. Phys. Chem. C*, 2018, **122**, 2712–2716.
- 18 E. Antolini, *Energy Environ. Sci.*, 2009, **2**, 915–931.
- 19 M. H. Seo, S. M. Choi, D. U. Lee, W. B. Kim and Z. Chen, *J. Power Sources*, 2015, **300**, 1–9.
- 20 M. V. Castegnaro, W. J. Paschoalino, M. R. Fernandes, B. Balke, M. C. M. Alves, E. A. Ticianelli and J. Morais, *Langmuir*, 2017, **33**, 2734–2743.
- 21 G. Bampos, S. Bebelis, D. I. Kondarides and X. Verykios, *Top. Catal.*, 2017, **60**, 1260–1273.
- 22 T. Gunji, R. H. Wakabayashi, S. H. Noh, B. Han, F. Matsumoto, F. J. DiSalvo and H. D. Abruña, *Electrochim. Acta*, 2018, **283**, 1045–1052.
- 23 M. H. Shao, T. Huang, P. Liu, J. Zhang, K. Sasaki, M. B. Vukmirovic and R. R. Adzic, *Langmuir*, 2006, **22**, 10409–10415.
- 24 D. Wang, H. L. Xin, H. Wang, Y. Yu, E. Rus, D. A. Muller, F. J. DiSalvo and H. D. Abruña, *Chem. Mater.*, 2012, **24**, 2274–2281.
- 25 K. Oishi and O. Savadogo, *J. Electroanal. Chem.*, 2013, **703**, 108–116.
- 26 M. R. Tarasevich, G. V. Zhutaeva, V. A. Bogdanovskaya, M. V. Radina, M. R. Ehrenburg and A. E. Chalykh, *Electrochim. Acta*, 2007, **52**, 5108–5118.
- 27 G. Jiang, H. Zhu, X. Zhang, B. Shen, L. Wu, S. Zhang, G. Lu, Z. Wu and S. Sun, *ACS Nano*, 2015, **9**, 11014–11022.
- 28 J. Liu, C. Q. Sun and W. Zhu, *Electrochim. Acta*, 2018, **282**, 680–686.
- 29 J. Wu, S. Shan, V. Petkov, B. Prasai, H. Cronk, P. Joseph, J. Luo and C. J. Zhong, *ACS Catal.*, 2015, **5**, 5317–5327.
- 30 T. H. Andriamiharintsoa, A. Rakotomahevitra, L. Piccolo and C. Goyhenex, *J. Nanopart. Res.*, 2015, **17**, 1–14.
- 31 T. Yang, Y. Ma, Q. Huang and G. Cao, *Nano Energy*, 2016, **19**, 257–268.
- 32 T. Yang, Y. Ma, Q. Huang, G. Cao, S. Wan, N. Li, H. Zhao, X. Sun and F. Yin, *Electrochem. Commun.*, 2015, **59**, 95–99.
- 33 H. Guo, H. Li, K. Jarvis, H. Wan, P. Kunal, S. G. Dunning, Y. Liu, G. Henkelman and S. M. Humphrey, *ACS Catal.*, 2018, **8**, 11386–11397.
- 34 P. Kunal, H. Li, B. L. Dewing, L. Zhang, K. Jarvis, G. Henkelman and S. M. Humphrey, *ACS Catal.*, 2016, **6**, 4882–4893.
- 35 S. García, L. Zhang, G. W. Piburn, G. Henkelman and S. M. Humphrey, *ACS Nano*, 2014, **11**, 11512–11521.
- 36 P. E. Blöchl, *Phys. Rev. B: Condens. Matter Mater. Phys.*, 1994, **50**, 17953–17979.
- 37 J. P. Perdew, K. Burke and M. Ernzerhof, *Phys. Rev. Lett.*, 1996, **77**, 3865–3868.
- 38 J. A. Pople, P. M. W. Gill and B. G. Johnson, *Chem. Phys. Lett.*, 1992, **199**, 557–560.
- 39 H. Monkhorst and J. Pack, *Phys. Rev. B: Solid State*, 1976, **13**, 5188–5192.
- 40 W. Tang, E. Sanville and G. Henkelman, *J. Phys.: Condens. Matter*, 2009, **21**, 084204.
- 41 A. R. Denton and N. W. Ashcroft, *Phys. Rev. A: At., Mol., Opt. Phys.*, 1991, **43**, 3161–3164.
- 42 H. Li, W. Chai and G. Henkelman, *J. Mater. Chem. A*, 2019, **7**, 23868–23877.
- 43 A. H. Larsen, J. J. Mortensen, J. Blomqvist, I. E. Castelli, R. Christensen, M. Dułak, J. Friis, M. N. Groves, B. Hammer, C. Hargus, E. D. Hermes, P. C. Jennings, P. B. Jensen, J. Kermode, J. R. Kitchin, E. L. Kolsbjerg, J. Kubal, K. Kaasbjerg, S. Lysgaard, J. B. Maronsson, T. Maxson, T. Olsen, L. Pastewka, A. Peterson, C. Rostgaard, J. Schiøtz, O. Schütt, M. Strange, K. S. Thygesen, T. Vegge, L. Vilhelmsen, M. Walter, Z. Zeng and K. W. Jacobsen, *J. Phys.: Condens. Matter*, 2017, **29**, 273002.
- 44 G. Schmid, M. Harms, J. O. Malm, J. O. Bovin, J. van Ruitenbeck, H. W. Zandbergen and W. T. Fu, *J. Am. Chem. Soc.*, 1993, **115**, 2046–2048.
- 45 N. Ortiz and S. E. Skrabalak, *Langmuir*, 2014, **30**, 6649–6659.
- 46 E. M. Fernández, P. G. Moses, A. Tofte Lund, H. A. Hansen, J. I. Martínez, F. Abild-Pedersen, J. Kleis, B. Hinnemann, J. Rossmeisl, T. Bligaard and J. K. Nørskov, *Angew. Chem., Int. Ed.*, 2008, **47**, 4683–4686.
- 47 B. Hammer and J. K. Nørskov, *Nature*, 1995, **376**, 238.
- 48 H. Xin, A. Vojvodic, J. Voss, J. K. Nørskov and F. Abild-Pedersen, *Phys. Rev. B: Condens. Matter Mater. Phys.*, 2014, **89**, 115114.
- 49 W. Chen and S. Chen, *J. Mater. Chem.*, 2011, **21**, 9169–9178.
- 50 F. Wang, K. Kusada, D. Wu, T. Yamamoto, T. Toriyama, S. Matsumura, Y. Nanba, M. Koyama and H. Kitagawa, *Angew. Chem., Int. Ed.*, 2018, **57**, 4505–4509.
- 51 G. Tofighi, X. Yu, H. Lichtenberg, D. E. Doronkin, W. Wang, C. Wöll, Y. Wang and J.-D. Grunwaldt, *ACS Catal.*, 2019, **9**, 5462–5473.
- 52 C. Weidenthaler, *Nanoscale*, 2011, **3**, 792–810.
- 53 H. Kobayashi, M. Yamauchi and H. Kitagawa, *J. Am. Chem. Soc.*, 2012, **134**, 6893–6895.
- 54 K. D. Gilroy, A. Ruditskiy, H. C. Peng, D. Qin and Y. Xia, *Chem. Rev.*, 2016, **116**, 10414–10472.
- 55 T. Mittermeier, A. Weiß, H. A. Gasteiger and F. Hasché, *J. Electrochem. Soc.*, 2017, **164**, F1081–F1089.
- 56 L. L. Fang, Q. Tao, M. F. Li, L. W. Liao, D. Chen and Y. X. Chen, *Chin. J. Chem. Phys.*, 2010, **23**, 543–548.
- 57 H. Erikson, A. Sarapuu, N. Alexeyeva, K. Tammeveski, J. Solla-Gullón and J. M. Feliu, *Electrochim. Acta*, 2012, **59**, 329–335.
- 58 E. Pizzutilo, S. Geiger, S. J. Freakley, A. Mingers, S. Cherevko, G. J. Hutchings and K. J. J. Mayrhofer, *Electrochim. Acta*, 2017, **229**, 467–477.
- 59 H. Li, S. Guo, K. Shin, M. S. Wong and G. Henkelman, *ACS Catal.*, 2019, **9**, 7957–7966.